

A Stability Result for Network Reduced Power Systems Using Virtual Friction and Inertia

Florian Reissner¹, Hang Yin², and George Weiss³

Abstract—We prove that virtual friction can stabilize a power grid containing several virtual synchronous machines (VSMs), connecting line impedances and loads. Virtual friction is a torque added to the swing equation of each VSM, proportional to the deviation of its frequency from the overall center of inertia (COI) frequency. Our analysis is based on the network reduced power system (NRPS) model. We support our results with simulations for a two-area network of four VSMs, looking at the transients induced by a change of tie-line impedance and an asymmetric load change. We compare the results for the NRPS model with the corresponding results using detailed models of synchronverters and line impedances. We find that virtual friction has a strong stabilizing effect both for the NRPS model and for the detailed model. Furthermore we show simulation results on the influence of time delays in the communication between the inverters. This communication is used to compute the COI frequency. It turns out that communication delays of less than 100ms have practically no effect on the overall system.

Index Terms—Power grid, virtual friction, virtual synchronous machine, exponential stability, NRPS model, Kuramoto model, frequency synchronization, inertia.

ABBREVIATIONS

COI	center of inertia
FEPS	friction enhanced power system
NK	nonlinear Kuramoto
NRPS	network reduced power system
SG	synchronous generator
VF	virtual friction
VSM	virtual synchronous machine.

I. INTRODUCTION

VIRTUAL synchronous machine (VSMs) are switched power converters that are controlled such that they mimic (towards the power grid) the behaviour of synchronous generators (SGs), providing frequency and

voltage droop as well as (virtual) inertia. They seem to be a very promising way for the development of inverters for the grid integration of distributed power generators, see for instance [3], [6], [17], [20], [22], [23], [28], [35], [42], [43]. VSMs are more flexible than SGs, as their parameters can be tuned and even changed on-line. Moreover, the frequency and voltage droops can act instantly, while in SGs connected to prime movers, they have large time constants. The main advantage of VSMs, as compared to current source inverters common in renewable energy sources, is that they can form stable grids, just like SGs. Their potential of providing grid frequency support by means of virtual inertia and frequency droop is shown, for instance, in [2], [14], [23], [24], [33]. Of course, the stability of a (micro)grid comprising VSMs, loads and transmission lines is not guaranteed, a careful analysis and parameter tuning are needed to achieve a stable grid. Thus, the stability analysis of power grids is an important and timely topic, see for instance [1], [4], [8], [9], [11], [13], [15], [18], [28], [31], [34], [39].

Investigating a single inverter connected to an infinite bus, [32] and [33] have proven almost global asymptotic stability based on hybrid angle control, a combination of DC-matching control and a non-linear angular damping feedback, based on angular differences modulo 4π . This type of control allows the phase differences of connected VSMs to reach and exceed 180° . The paper [29] investigates the stability of grids where several VSMs are operated in parallel, by means of μ -analysis. The paper [5] investigates the stability of a power network employing VSMs based on the singular perturbation method, separating the system dynamics into slow, fast and very fast dynamics. It derives sufficient stability conditions for the inverter parameters to guarantee stability of such a network.

A major issue with VSMs employing frequency droop control is that they have to inject large excess power during disturbances where the grid frequency drops below its nominal value. Hardware power ratings of the electronic components and/or the limited availability of excess DC power impose an upper bound for the frequency droop constant and/or they force the droop torque to saturate, which is bad for stability. To avoid reaching saturation frequently, the frequency droop constant (per unit) employed in inverters is typically much smaller than that imposed on the prime mover of an SG [22].

VSMs open up entirely new avenues for grid stabilization, that are not possible with SGs: In order to decouple stability requirements from hardware requirements, we propose to introduce **virtual friction (VF)**, as an additional viscous friction torque, acting on the virtual rotors of the connected VSMs.

Manuscript received June 27, 2021; revised October 27, 2021; accepted December 26, 2021. Date of publication December 31, 2021; date of current version April 22, 2022. This work was supported by the Israeli Ministry of Infrastructure, Energy, and Water under Grant 219-11-128. The work of Florian Reissner was supported by the European Union's Horizon 2020 Research and Innovation Program through the Marie Skłodowska-Curie under Grant 861398. Paper no. TSG-01019-2021. (*Corresponding author: Florian Reissner.*)

The authors are with the School of Electrical Engineering, Tel Aviv University, Ramat Aviv 69978, Israel (e-mail: reissner@tauex.tau.ac.il; yinhang5281@gmail.com; gweiss@tauex.tau.ac.il).

Color versions of one or more figures in this article are available at <https://doi.org/10.1109/TSG.2021.3139165>.

Digital Object Identifier 10.1109/TSG.2021.3139165

This torque employs the COI frequency as a reference. (The concept of COI has been introduced in [30] and has been used extensively, see for instance [41].) VF has been introduced in [7] and [38] but only for two VSMs (or two areas), so that the friction torque is proportional to the difference in frequency between these two, without the need for the COI frequency. Simulation experiments in [7] show that VF greatly enhances the stability of a two-area power system with weak links between the two areas. In damping oscillations, the effect of VF is similar to that of the frequency droop, but without the need to inject large excess power if the grid frequency is below the nominal value. The paper [12] has extended this concept and implemented VF using PID-controllers. The authors show that this control can compensate for communication delays to some extent. From pole zero plots of the linearized equation, it becomes clear that the strongest damping effect can be achieved by increasing the proportional gain of the controllers.

It is important to state that the calculation of the COI frequency requires the transmission of angular velocity information of the VSMs across the power network. The transmission time delays that occur in the communication infrastructure complicate the stability analysis of such systems. In particular, time delays may not be constant over time and may have different values for each communication link, see for example [26] for a stochastic modelling of time delays. In a real grid, time delays may be due to (see [40]):

- *Transmission Delay*: Time a packet needs for transmission via the employed protocol, dependent on the bandwidth.
- *Propagation Delay*: Time for the data to propagate through the medium (copper wire or fiber optic cable).
- *Processing Delay*: Time required by the data acquisition unit to prepare and send a frame + time required by the VSM to receive and decode the received data.

In order to bypass time delays, a decentralized approach was proposed in [9], where an additional control loop is implemented in the VSM algorithm, based on angular acceleration and active power output. A small-signal approach is used to tune the control parameters. In order to understand the impact of time delay on the VF mechanism, we have conducted exhaustive simulations. Our surprising conclusion is that the system behaviour remains largely unchanged for constant but not necessarily equal time delays up to around 100ms, at least for the simple two area grid with 4 VSMs studied in this paper.

The stability analysis of larger power grids must of course involve simplified models of the generators, transmission lines and loads, because working with full models (high order non-linear systems) makes any analysis intractable, see for instance [27], [36]. An important and successful direction of research in this field has been the study of the NRPS model (see [11], [15], and [30]) and its inertia-less limit version, the nonlinear Kuramoto (NK) model. In the NRPS model, each generator is represented by a system of order two (the swing equation) and the transmission lines and loads are static and are represented by complex impedances without state variables. Stability results for the NK and NRPS models have been derived in [15] and improved in [37]. They give-under reasonable assumptions on the impedances of the power network and

for small enough inertias-a local exponential stability result on the grounded rotor angles of the synchronous generators in the network.

In this paper we extend the NRPS model by incorporating VF. In [15] and in the stronger version of the main result that is in [37], it was proven that, under suitable assumptions, the NRPS model becomes stable if the inertias of the generators are sufficiently small. However, making the inertias very small comes at a price: The system frequency will vary a lot more and much faster. The advantage of VF is that we no longer have to make the inertia terms small, instead, to achieve stability, it suffices to increase the VF coefficients. We test VF in simulations of a micro grid, using high models for every component, and we also test the corresponding reduced model which is the NRPS model. For each of the two models (the high order and the reduced one) we simulate a change of tie-line impedance between two areas, as well as an asymmetric change of load, and we observe the resulting transients with and without VF. Our results show that indeed, the addition of VF stabilizes the system even if the network is chosen such that it is unstable without the additional damping term. Moreover, with VF, the transients decay much faster. This paper is structured as follows: In Section II we recall the NK and NRPS models and we introduce the new model that has VF. We also state the stability result for the model with VF. Section III contains the proof for the main theorem of this paper, in which we consider separately the dynamics of the COI frequency and then we show that, on a different time scale, the new model with VF reduces to the NK model. This allows us to perform a singular perturbation analysis, as in [37]. An interpretation of the theorem in the context of power systems is given in Section IV. In Section V we report our simulations, that show the influence of the VF torques on the second order SG models and compare the evolution of the grounded rotor angles for the same scenarios of the grid. In addition, a more realistic simulation based on the synchronverter detailed in [20], [21] is performed on the same grid, also employing a more detailed dynamic model for the transmission lines and resistive loads. Finally we investigate the impact of the communications time delays on the stabilizing effect of the VF.

II. POWER FLOW MODEL WITH VIRTUAL FRICTION

Notation: We follow the notation from [37] (see also [15]). We represent all angles on the unit circle \mathbb{T} by numbers in $(-\pi, \pi]$ (modulo 2π). Addition and subtraction are performed modulo 2π . For two angles $\theta_1, \theta_2 \in \mathbb{T}$ the *geodesic distance* between them is

$$|\theta_1 - \theta_2|_g = \min\{|\theta_1 - \theta_2|, 2\pi - |\theta_1 - \theta_2|\}.$$

Let $n \in \mathbb{N}$ be fixed. For any $\gamma \in (0, \pi]$ we define

$$\Delta(\gamma) = \left\{ \theta \in \mathbb{T}^n \mid \exists \theta_0 \in \mathbb{T} \text{ } ||\theta_j - \theta_0|_g < \frac{\gamma}{2}, 1 \leq j \leq n \right\}.$$

The statement $\theta \in \Delta(\gamma)$ means that there exists an open arc of length γ in \mathbb{T} that contains all the angles θ_j . For $\gamma \in (0, \pi]$ we define $\overline{\Delta}(\gamma)$ as the closure of $\Delta(\gamma)$ in \mathbb{T}^n . As in [15],

we introduce the mapping $\text{grnd} : \mathbb{T}^n \rightarrow \mathbb{R}^{n-1}$ as $\delta = \text{grnd}(\theta)$ where:

$$\delta_j = \theta_j - \theta_n, \quad 1 \leq j \leq n-1. \quad (1)$$

The above representation of angle differences loses one degree of freedom, since for n angles $n-1$ differences are defined. Where required in the following, $\delta_n = 0$. For any $\gamma \in (0, \pi]$ the grounded set $\Delta_{\text{grnd}}(\gamma) \subset \mathbb{R}^{n-1}$ is defined as:

$$\Delta_{\text{grnd}}(\gamma) = \left\{ \delta \in \mathbb{R}^{n-1} \mid \begin{array}{l} |\delta_j| < \gamma, \\ |\delta_j - \delta_k| < \gamma, \end{array} \quad 1 \leq j, k \leq n-1 \right\}.$$

We denote the closure of this grounded set by $\bar{\Delta}_{\text{grnd}}(\gamma)$.

Parameters of the Models: The matrix $[a_{jk}] \in \mathbb{R}^{n \times n}$ is such that

$$a_{jk} = a_{kj} > 0 \quad \text{for} \quad 1 \leq j, k \leq n, \quad j \neq k$$

and $a_{jj} = 0$ for $j \in \{1, \dots, n\}$. We define an array of phase shifts $\varphi_{jk} \in \mathbb{T}$ that satisfies

$$\varphi_{jk} = \varphi_{kj} \in \left(-\frac{\pi}{2}, \frac{\pi}{2}\right) \quad \text{for} \quad 1 \leq j, k \leq n, \quad j \neq k.$$

The diagonal values φ_{jj} are not relevant. In our application, we need these parameters to describe the electric network connecting n VSMs. For their precise physical interpretation, see Section IV. We also introduce four sets of n real numbers: $M_j > 0, D_j > 0, F_j > 0$ and $p_j \in \mathbb{R}, j \in \{1, 2, \dots, n\}$.

The *NK model* is a collection of n first order differential equations on \mathbb{T}^n , defined for $1 \leq j \leq n$. It has been proposed in [15] as an extension to the Kuramoto model, describing synchronization between a set of coupled oscillators connected through a lossy network:

$$D_j \dot{\theta}_j = p_j - \sum_{k=1}^n a_{jk} \sin(\theta_j - \theta_k - \varphi_{jk}).$$

The state of this system is $\theta = (\theta_1, \dots, \theta_n)$, which evolves in the state space \mathbb{T}^n . We denote $\omega_j = \dot{\theta}_j$.

As a simplified model describing a power network, the **NRPS model** has been derived in [30] (see also [10, Ch. 6] and [37]). In this model, n SGs are connected via a passive network and $\theta_1, \dots, \theta_n$ are the rotor angles of the generators. The model consists of n second order differential equations on \mathbb{T} : for $1 \leq j \leq n$,

$$M_j \ddot{\theta}_j + D_j \dot{\theta}_j = p_j - \sum_{k=1}^n a_{jk} \sin(\theta_j - \theta_k - \varphi_{jk}). \quad (2)$$

We will refer to M_j as *inertia terms*, to D_j as *damping coefficients* and to p_j as *power terms*. The precise connection between these parameters and the parameters of an electric grid is derived in [37, Sec. 3]. Let us denote $\omega_j = \dot{\theta}_j$. The state of the dynamical system (2) is:

$$(\theta, \omega) = (\theta_1, \dots, \theta_n, \omega_1, \dots, \omega_n) \in \mathbb{T}^n \times \mathbb{R}^n, \quad (3)$$

where, again, $\omega_j = \dot{\theta}_j$. Let ω_c be the *center of inertia frequency*, defined as in [30]:

$$\omega_c = \frac{\sum_{k=1}^n M_k \omega_k}{\sum_{k=1}^n M_k}. \quad (4)$$

In this paper we are interested in a modification of the NRPS model, where a new viscous friction term $F_j(\omega_j - \omega_c)$ is added to the left-hand side of (2). This leads to:

$$M_j \ddot{\theta}_j + (D_j + F_j) \dot{\theta}_j = \tilde{p}_j - \sum_{k=1}^n a_{jk} \sin(\theta_j - \theta_k - \varphi_{jk}),$$

where

$$\tilde{p}_j = p_j + F_j \omega_c. \quad (5)$$

We will refer to F_j as a *virtual friction coefficient*. We assume that the ratios of damping and virtual friction coefficients over inertia terms are the same for all the VSMs in the network. This enables us to define the parameters d and f as:

$$d = \frac{D_j}{M_j}, \quad f = \frac{F_j}{M_j}, \quad 1 \leq j \leq n. \quad (6)$$

Note that the actual values of d and f would be defined beforehand according to the grid's requirements and individual inverters would be configured to fulfil this requirement prior to their integration into the grid. With the above, we define the following model that we shall call the *friction enhanced power system (FEPS) model*:

$$M_j \ddot{\theta}_j + M_j(d + f) \dot{\theta}_j = \tilde{p}_j - \sum_{k=1}^n a_{jk} \sin(\theta_j - \theta_k - \varphi_{jk}). \quad (7)$$

The state of the system (7) is again defined as in (3).

In the following, we show the improved stability properties of this model over the NRPS model. For this, we impose the exact same assumptions on the parameters D_j, p_j, a_{jk} and φ_{jk} as in the main result of [37].

Theorem 1: Consider the system (7), with state (θ, ω) , where $\omega = \dot{\theta}$, with \tilde{p} defined as in (5). Denote

$$\varepsilon = \frac{1}{(d + f)^2}, \quad (8)$$

and define:

$$\begin{aligned} \Gamma_{\min} &= n \min_{j \neq k} \left\{ \frac{a_{jk}}{D_j} \cos \varphi_{jk} \right\}, \quad \varphi_{\max} = \max_{j \neq k} \{ |\varphi_{jk}| \}, \\ \Gamma_{\text{crit}} &= \frac{1}{\cos \varphi_{\max}} \left(\max \left| \frac{p_j}{D_j} - \frac{p_k}{D_k} \right| + 2 \max_{1 \leq j \leq n} \sum_{k=1}^n \frac{a_{jk}}{D_j} \sin \varphi_{jk} \right). \end{aligned}$$

Assume that

$$\Gamma_{\min} > \Gamma_{\text{crit}}. \quad (9)$$

Define $\gamma_{\min} \in [0, \frac{\pi}{2} - \varphi_{\max})$ as the unique solution of

$$\sin \gamma_{\min} = \frac{\Gamma_{\text{crit}}}{\Gamma_{\min}} \cos \varphi_{\max},$$

and set $\gamma_{\max} = \pi - \gamma_{\min}$. Then there exists a unique point with $\delta^* = (\delta_1^*, \dots, \delta_{n-1}^*) \in \bar{\Delta}_{\text{grnd}}(\gamma_{\min})$ with the following properties:

For every $\gamma_0 \in (\gamma_{\min}, \gamma_{\max})$ and every $\omega_{\max} > 0$ there exists a constant $\varepsilon_* > 0$ such that if $0 < \varepsilon < \varepsilon_*$, then for any initial state $(\theta(0), \omega(0))$ satisfying

$$\theta(0) \in \bar{\Delta}(\gamma_0), \quad \|\omega(0)\| \leq \omega_{\max}, \quad (10)$$

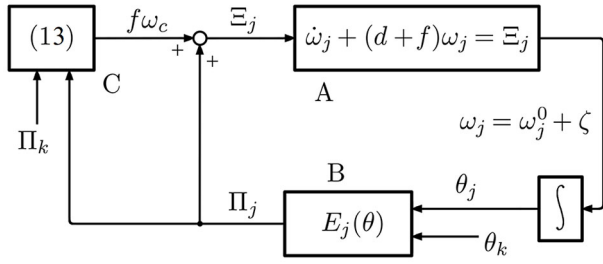


Fig. 1. A possible representation of the FEPS model. The analysis is greatly simplified by the observation that the scalar signal $f\omega_c$ has no influence on the signals Π_j that come out of the blocks B .

the following holds for all $j \in \{1, 2, \dots, n-1\}$:

$$\lim_{t \rightarrow \infty} [\theta_j(t) - \theta_n(t)] = \delta_j^*, \quad \lim_{t \rightarrow \infty} \omega_j(t) = \omega^*,$$

where

$$\omega^* = \frac{1}{D_j} \left(p_j - \sum_{k=1}^n a_{jk} \sin(\delta_j^* - \delta_k^* - \varphi_{jk}) \right).$$

This theorem shows that for the FEPS model, if the same assumptions hold as in the main result of [37], then the model can be made stable by increasing the VF coefficients (instead of reducing the inertia terms).

III. THE PROOF OF THEOREM 1

Before giving the formal proof, we illustrate an important idea at its core, which is the isolation of the coupling term $f\omega_c$ in the model (7) (it is part of \tilde{p}_j/M_j). For this, we give a representation where the influence of this term can be linearly superposed with the solution of the same model where this term is deleted. We work under the assumption (6). We represent equation (7) as a block diagram in Fig. 1. The block B is the following nonlinear function:

$$\Pi_j = E_j(\theta) = \frac{p_j}{M_j} - \frac{1}{M_j} \sum_{k=1}^n a_{jk} \sin(\theta_j - \theta_k - \varphi_{jk}).$$

Subsystem A is a stable first order linear differential equation with input $\Xi_j = f\omega_c + \Pi_j$. Subsystem C outputs $f\omega_c$, which is the solution of the first order linear (stable) differential equation (13). The output of block A can be written as the superposition of two variables: ω_j^0 that corresponds to the input Π_j and the true initial state $\omega_j(0)$, and ζ that corresponds to the input $f\omega_c$, and the initial state zero (for subsystem A). Note that ζ is the same for all VSMs, i.e., for each index j . The important observation is that the output of block B depends solely on angular differences, such that ζ (and hence also $f\omega_c$) has no impact on Π_j . Subsystem C is a first order stable differential equation, depending on a weighted average of the signals Π_j , which, as we just saw, does not depend on $f\omega_c$. We conclude that the model does not contain any closed loop for the variable $f\omega_c$. Employing known stability results for the model with $f\omega_c = 0$, we can conclude stability for (7) without the impact of VF. This shows that in case of stability, also $f\omega_c$ will not destabilize the model and converge to some constant. The formal proof follows.

Step 1: The COI frequency ω_c is a function of the frequencies ω_j . To analyse the system stability, we have to investigate the stability of ω_c . By differentiating (4) and using (7), we obtain that

$$\begin{aligned} \left(\sum_{k=1}^n M_k \right) \dot{\omega}_c &= \sum_{k=1}^n M_k \dot{\omega}_k \\ &= \sum_{j=1}^n M_j [-d\omega_j + f(\omega_c - \omega_j)] \\ &\quad + \sum_{j=1}^n [p_j - P_{e,j}(\theta)], \end{aligned} \quad (11)$$

where $P_{e,j}(\theta)$ is defined by

$$P_{e,j}(\theta) = \sum_{k=1}^n a_{jk} \sin(\theta_j - \theta_k - \varphi_{jk}), \quad (12)$$

and its interpretation is the electrical power output of VSM j . By the definition of ω_c , $\sum_{j=1}^n M_j(\omega_c - \omega_j) = 0$. Thus (11) can be written as:

$$\left(\sum_{k=1}^n M_k \right) \dot{\omega}_c = -d \sum_{j=1}^n M_j \omega_j + \sum_{j=1}^n [p_j - P_{e,j}(\theta)].$$

Dividing by $\sum_{k=1}^n M_k$ gives a first order linear differential equation:

$$\dot{\omega}_c = -d\omega_c + \frac{\sum_{j=1}^n [p_j - P_{e,j}(\theta)]}{\sum_{k=1}^n M_k}, \quad (13)$$

which shows that ω_c converges to some limit ω_c^* if the functions $P_{e,j}(\theta)$ converge to some limits.

Step 2: The FEPS model (7) corresponds to the NRPS model with the additional disturbance term $f\omega_c$ and an enhanced damping coefficient $M_j(f+d)$ (in place of $M_j d$).

Lemma 1: Let (θ, ω) be a solution of (7). Let (θ^0, ω^0) be the solution of the related equation

$$M_j \ddot{\theta}_j^0 + M_j(d+f)\dot{\theta}_j^0 = p_j - P_{e,j}(\theta^0), \quad (14)$$

where $P_{e,j}(\theta^0)$ is defined as in (12) and $\omega_j^0 = \dot{\theta}_j^0$, starting from the same initial conditions:

$$\omega_j^0(0) = \omega_j(0), \quad \theta_j^0(0) = \theta_j(0).$$

Denote $\zeta = \omega_j - \omega_j^0$. Then the function ζ is independent of j and it is the unique solution of

$$\dot{\zeta} + (d+f)\zeta = f\omega_c, \quad (15)$$

starting from $\zeta(0) = 0$, where ω_c is defined in (4).

Notice that the only real difference between the equations (7) and (14) is that \tilde{p}_j has been replaced with p_j .

Proof of Lemma 1: Let ζ be the solution of (15) for the given function ω_c , starting from $\zeta(0) = 0$, i.e.,

$$\zeta(t) = \int_0^t e^{-(d+f)(t-\sigma)} f\omega_c(\sigma) d\sigma.$$

Let (θ^0, ω^0) be the solution of (14) starting from the same initial condition as (θ, ω) , as defined in the lemma. We define (θ^1, ω^1) by

$$\omega_j^1 = \omega_j^0 + \zeta, \quad \theta_j^1(t) = \theta_j^0(t) + \int_0^t \zeta(\sigma) d\sigma. \quad (16)$$

Note that $\theta_j^1(t) - \theta_k^1(t) = \theta_j^0(t) - \theta_k^0(t)$, so that for all $j, k \in \{1, 2, \dots, n\}$,

$$P_{e,j}(\theta^1) = P_{e,j}(\theta^0). \quad (17)$$

It follows from (14), (15), (16) and (17) that

$$\begin{aligned} \dot{\omega}_j^1 &= \dot{\omega}_j^0 + \dot{\zeta} \\ &= -(d+f)\omega_j^0 + \frac{p_j}{M_j} - \frac{P_{e,j}(\theta^0)}{M_j} - (d+f)\zeta + f\omega_c \\ &= -(d+f)\omega_j^1 + \frac{p_j}{M_j} - \frac{P_{e,j}(\theta^1)}{M_j} + f\omega_c, \end{aligned} \quad (18)$$

i.e., ω^1 and θ^1 satisfy (7). Moreover, since $\omega^1(0) = \omega(0)$ and $\theta^1(0) = \theta(0)$, we obtain that

$$\omega^1(t) = \omega(t) \quad \theta^1(t) = \theta(t) \quad \forall t \geq 0. \quad (19)$$

Hence, we have indeed $\zeta = \omega_j - \omega_j^0$, for all $j \in \{1, 2, \dots, n\}$. ■

Step 3: We introduce new variables $x_j (j \in \{1, 2, \dots, n\})$ and a new timescale τ as follows:

$$\tau = \frac{1}{\beta}t, \quad x_j = \beta\omega_j^0, \quad \beta > 0.$$

Substituting for t and ω_j^0 in (14) gives:

$$\frac{M_j}{\beta^2} \frac{d}{d\tau} x_j + M_j \frac{d+f}{\beta} x_j = p_j - P_{e,j}(\theta).$$

We choose $\beta = d+f$ so that $\varepsilon = \frac{1}{\beta^2}$ by (8). This allows rewriting equation (14) in the form of a standard perturbation problem with ε as the singular perturbation parameter:

$$\begin{aligned} \varepsilon M_j \frac{d}{d\tau} x_j &= -M_j x_j + p_j - \sum_{k=1}^n a_{jk} \sin(\theta_j^0 - \theta_k^0 - \varphi_{jk}), \\ \frac{d}{d\tau} \theta_j^0 &= x_j. \end{aligned}$$

For $\varepsilon \rightarrow 0$, the reduced system dynamics are given by:

$$M_j x_j = p_j - \sum_{k=1}^n a_{jk} \sin(\theta_j^0 - \theta_k^0 - \varphi_{jk}). \quad (20)$$

Note that this equation is of identical structure as the NK model. Writing the above using the grounded angles from equation (1) gives for $1 \leq j \leq n$:

$$\begin{aligned} M_j \varepsilon \frac{d}{d\tau} x_j &= -M_j x_j + p_j - \sum_{k=1}^n a_{jk} \sin(\delta_j - \delta_k - \varphi_{jk}), \\ \frac{d}{d\tau} \delta_j &= x_j - x_n, \end{aligned} \quad (21)$$

where we have used that $\delta_j = \theta_j^1 - \theta_n^1 = \theta_j^0 - \theta_n^0$, according to (16) and (19). The equations (21) are now of the same form

as the equations (19), (20) from [37], with x_j in place of ω_j , and with M_j in place of m_j and also in place of D_j from [37].

Thus we can apply Theorem 4.1 from [37] to conclude that there exist suitable conditions (as stated in Theorem 1) for which the following holds:

$$\omega_j^0 \rightarrow \omega^{0*}, \quad \delta_j \rightarrow \delta_j^*.$$

It follows thus with (12) that $P_{e,j}(\delta) \rightarrow P_{e,j}(\delta^*)$. According to (13) the COI frequency converges, $\omega_c \rightarrow \omega_c^*$, and therefore also the solution of (15) converges:

$$\zeta(t) \rightarrow \zeta^*.$$

With Lemma 1 we get that $\omega_j \rightarrow \omega^* = \omega^{0*} + \zeta^*$

IV. DISCUSSION OF THE THEOREM

Theorem 1 gives sufficient conditions under which the FEPS model can be made asymptotically stable by choosing large enough VF coefficients. Here we give an interpretation of the theorem in the context of power systems.

Consider a network connecting n VSMs via linear passive circuit elements (this network may include loads). Denote by $Y = [Y_{jk}]$ the admittance matrix of the network connecting the VSMs. We assume that the frequencies of all the VSMs are very close to a nominal frequency ω_{nom} , so that Y can be regarded as a constant (complex) matrix. We denote by E_j the amplitude of the voltage generated by VSM j , which is assumed to be constant. Of course, these are approximations made in order to get a model of manageable complexity, namely the NRPS model.

Now the parameters a_{jk} and φ_{jk} from the NRPS and FEPS models are obtained as follows:

$$a_{jk} = E_j E_k |Y_{jk}|, \quad \forall j, k \in \{1, 2, \dots, n\}, \quad j \neq k,$$

$a_{jj} = 0$ and $\varphi_{jk} + \frac{\pi}{2}$ is the angle of Y_{jk} . For the details of how this model is derived, we refer to [37, Sec. 3]. φ_{jk} can be regarded as a measure of the losses of the network (the power consumption of the loads is included in these losses). Indeed, for a purely inductive network, we would have $\varphi_{jk} = 0$. A network is called *predominantly inductive* if $|\varphi_{jk}| < \frac{\pi}{2}$ for all $j \neq k$. The entry a_{jk} expresses how strongly the VSMs j and k are connected. The term p_j depends on the set point $P_{set,j}$ for the power of VSM j , as follows:

$$p_j = P_{set,j} + D_j \omega_{nom} + E_{jj}^2 |Y_{jj}| \sin \varphi_{jj}.$$

The term $E_{jj}^2 |Y_{jj}| \sin \varphi_{jj}$ is the power that VSM j would inject into the grid if all the other VSMs were short circuited.

The main condition of the theorem, (9) gives some requirement on the grid and VSMs, which can be interpreted as follows: The term $\max |\frac{p_j}{D_j} - \frac{p_k}{D_k}|$ evaluates the non-uniformity of the VSMs. The expression $n \min_{j \neq k} \{\frac{a_{jk}}{D_j} \cos \varphi_{jk}\}$ is the minimal connectivity between two VSMs where $a_{jk} \cos \varphi_{jk}$ is proportional to the imaginary part of Y_{jk} . Finally,

$$2 \max_{1 \leq j \leq n} \sum_{k=1}^n \frac{a_{jk}}{D_j} \sin \varphi_{jk}$$

can be interpreted as a measure of power exchange between the VSMs, scaled by the VSM's droop constants.

In the FEPS model $D_j = dM_j$ and $F_j = fM_j$, which allows us to replace D_j in the expressions for Γ_{crit} and Γ_{min} by M_j . This is possible since both sides of (9) get scaled by the same factor. Note that (9) can only be satisfied for a fully connected network ($a_{jk} \neq 0 \ \forall j \neq k$). Recall the definition of $\Delta(\gamma)$ as the set of angles contained in an open arc of length $\gamma \leq \pi$. Denote the maximum geodesic distance between two angles of the set $\{\theta_1, \theta_2, \dots, \theta_n\}$ by

$$V(\theta(t)) = \left\{ \max |\theta_j(t) - \theta_k(t)|_g \mid j, k \in \{1, \dots, n\} \right\}.$$

In [15] it is shown that the upper Dini derivative of $V(\theta(t))$ satisfies

$$D^+V(\theta(t)) \leq \Gamma_{crit} \cos \varphi_{max} - \Gamma_{min} \sin \gamma.$$

Inequality (9) is obtained by requiring that $D^+V(\theta(t)) < 0$.

The terms Γ_{crit} , Γ_{min} and $\cos \varphi_{max}$ depend on the power network and the inverter settings which can be assumed to be constant in our analysis. $D^+V(\theta(t))$ is negative for $\theta \in \Delta(\gamma)$ if $\gamma \in (\gamma_{min}, \gamma_{max})$ and for $\theta(0) \in \bar{\Delta}(\gamma)$ the maximum geodesic distance between two angles in θ decreases at least until it reaches γ_{min} .

We analyse in the following how the parameters of the reduced model (20) impact the contraction speed of $V(\theta(t))$ and the region where the theorem predicts stability, delimited by γ_{max} . The following table summarizes the influences of the different terms in Γ_{crit} and Γ_{min} :

	γ_{max}	$-D^+V(\theta(t))$
more uniform settings $\frac{p_j}{D_j}$	+	+
more uniform coupling $\frac{a_{jk}}{D_j}$	+	+
lower network losses φ_{jk}	+	+
higher damping D_j or F_j	=	-

The first two lines of the table refer to the uniformity of the network and the VSMs. Note that the ratio $\frac{\Gamma_{crit}}{\Gamma_{min}}$ increases if the values $\frac{a_{jk}}{D_j}$ are more uneven. This is true since for a set of n different real numbers z_j , $\sum z_j \geq n \min(z_j)$. Higher uniformity of both $\frac{p_j}{D_j}$ and $\frac{a_{jk}}{D_j}$ has a positive impact on the region of attraction of the equilibrium point and the contraction speed of $V(\theta)$. Recall that φ_{jk} is zero for a purely inductive admittance between VSMs j and k . Increasing φ_{jk} decreases Γ_{min} and increases Γ_{crit} . Interestingly, increasing D_j or F_j decreases the rate of contraction of $V(\theta)$ while-as stated above-does not impact γ_{max} . Note that the above analysis is valid for the reduced model (20).

Simulations with the FEPS model and also with the detailed model of the same grid show that VF strongly increases the convergence rate of ω_j towards (not necessarily constant) ω_c and also strongly dampens the oscillations between the VSMs, as shown for a two area grid in the next section. The value for f used in the simulations in Section V was empirically chosen to maximize the convergence speed of ω_j towards ω_c and of δ to a steady state. Our results show that (in the case of a stable system) the settling time of the VSMs subsequent to a disturbance is in the range of 10s for both cases, VF active

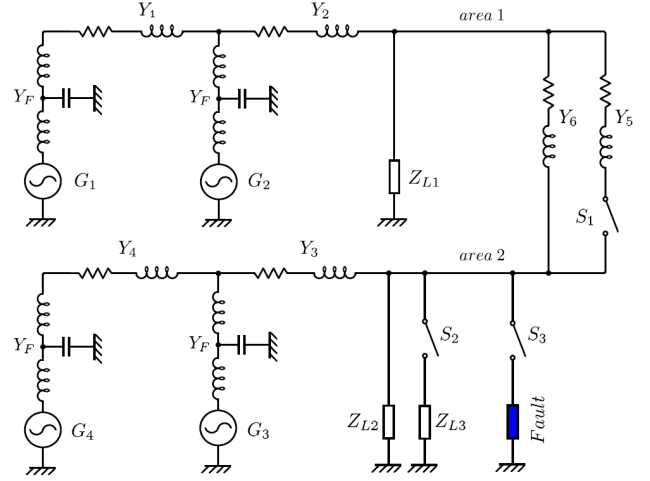


Fig. 2. Simulated two area grid with four VSMs (3 phase grid). Switch S_1 is used to change the line impedance between the two areas and S_2 is used to connect load L_3 . Closing S_3 simulates a 3 line fault.

and VF inactive. This suggests that the chosen value of f is high enough to suppress oscillations, but small enough to not slow down the system's behaviour.

For more on the significance of the parameters discussed here, we refer the interested reader to the survey on the synchronization of the NK and NRPS models in [16].

V. SIMULATION RESULTS

Here we present simulation results for a two area network where each area consists of two VSMs and one load (see Fig. 2). An additional load L_3 in parallel with load L_2 serves to introduce a load step change in area 2. The line impedance between the two areas can be changed by operating switch S_1 , (dis-)connecting transmission line Y_5 . We present the simulations based on the detailed VSM algorithm from [19], [20], [25] with a dynamic network model, as well as results for the NRPS and FEPS models. All simulations were conducted in the MATLAB/Simulink environment.

A. The Detailed Model

The VSM algorithm was run at 10kHz while the power part is simulated at a step size corresponding to 100kHz. We use the ode4 (Runge-Kutta) solver for these simulations. Loads are modelled as constant impedance and transmission lines as RL circuits. Switches in the model have negligible breaker resistance and snubber resistance of 1k Ω and snubber capacitance of 200nF. All synchronverters have nominal power 9kW and have identical parameters with $M_j = 188.5 \text{ Ws}^2$ and $D_j = 94.2 \text{ Ws}$ and $F_j = 3141.6 \text{ Ws}$. The set powers of all inverters were $P_{set} = 5 \text{ kW}$ and $Q_{set} = 0 \text{ kVar}$.

In this paper, simulations employ a 1ms round trip time delay for the transmission of COI frequency data between the inverters and the central processor. The transmission network admittances Y_1 to Y_5 consist of $R = 0.1\Omega$ and $L = 1\text{mH}$ and Y_6 is equivalent to $R = 10\Omega$ and $L = 100\text{mH}$. The inverter outputs are connected to symmetric LCL-filters Y_F with each coil $L = 1.1\text{mH}$, $R = 0.1\Omega$ and a capacitor of $C = 20\mu\text{F}$. These filters are parts of our network. Loads 1 and 2 consume

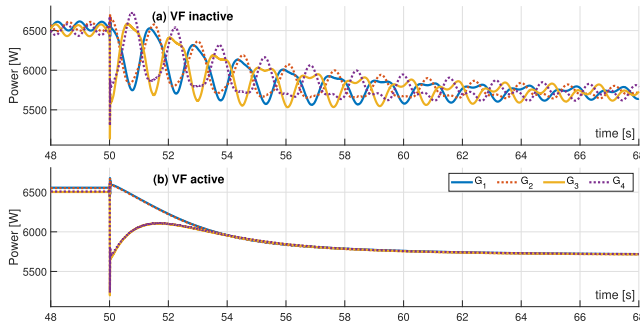


Fig. 3. Active power output following the disconnection of load L_3 starting at $t = 50$ s. Subfigure (a) shows the plots without VF, while subfigure (b) shows the much smoother transition with VF.

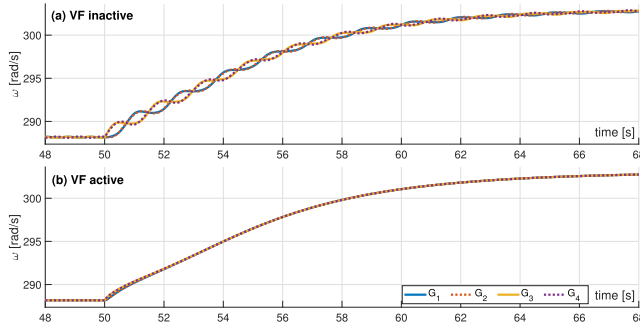


Fig. 4. Frequencies following the disconnection of load L_3 starting at $t = 50$ s. (a) Slowly decaying oscillations between the two areas are observed without VF. (b) VF effectively suppresses oscillations. Minimal differences between the frequencies can be observed in the first 2s.

12kW active power, while load L_3 consumes 5kW. No reactive power is consumed by the loads. We use a reactive power control loop as in [20], [25] and we inject random current and voltage measurement errors of a realistic size and power spectral density, see [20] for the details. As the transmission line impedance between the two VSMs within the same area is relatively low, their coupling is strong. Simulation results show that the effect of VF is beneficial when the load imbalance between the two areas is large and a strong tie line current is required to balance the two areas. In the case where the two areas are relatively balanced and therefore almost zero power flow is required between the two areas, a change in tie line impedance has little effect, as expected. The largest benefit of VF is observed in the following two scenarios:

- The tie line impedance is high and a sudden change in load occurs in one of the two areas.
- The tie line impedance sees a step change at a high load imbalance.

We describe our results for these two scenarios.

1) Step Down Change in Load at High Tie Line Impedance:

Figures 3 and 4 show simulation results for the four VSMs after a sudden disconnection of load L_3 leading to a step change of the active power consumption in area 2 at $t = 50$ s. This change occurs when switch S_1 is open, thus at a weak tie line between the two areas. When the VF is inactive, the active power output of the two VSMs in area 2 suddenly decreases by about 900W, whereas the two VSMs of area 1 initially only see a small disturbance. However, poorly damped oscillations between the two areas with a frequency of 0.64Hz are induced

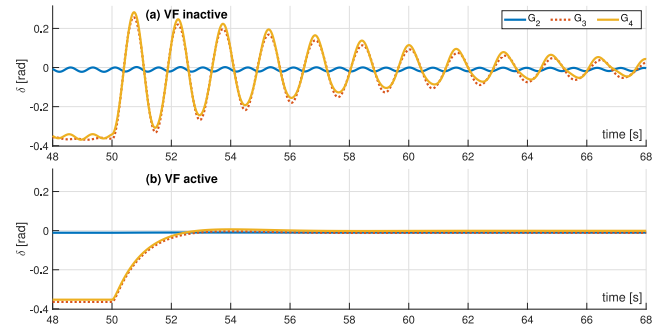


Fig. 5. Grounded rotor angles with respect to VSM G_1 , following the disconnection of load L_3 starting at $t = 50$ s. (a) Oscillations occur only without VF. (b) Transients with VF last for about 4 seconds.

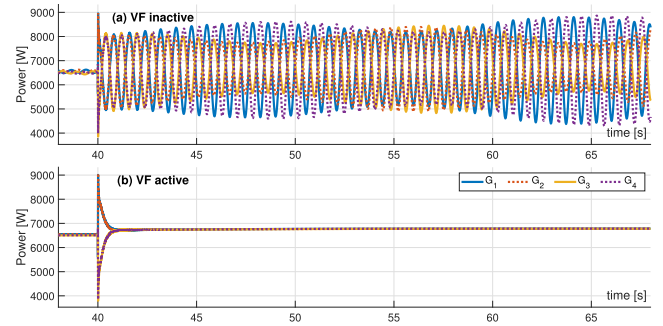


Fig. 6. Active power output following a tie-line impedance step down starting at $t = 40$ s. (a) Several frequencies are observed when VF is inactive. (b) Transients are non oscillatory and decay quickly when VF is active.

(See Fig. 3a). These oscillations do not occur when the VF is active (see Fig. 3b). Instead, within 3 seconds, the power output of the 4 VSMs converges without oscillations to equal values. In both cases, the overall active power output of all four VSMs has a transient lasting for about 10s.

Fig. 4 shows the VSM frequencies for the same experiment with and without VF. In both cases, the frequency of the four VSMs increases at a slower rate dictated by the rate of change of the excitation current control (see [25]). The inter area oscillations show as modulations of the VSM frequencies with an initial amplitude of 1 rad. These are fully damped when VF is active.

Fig. 5 shows the grounded angles of VSMs G_2 to G_4 with respect to VSM G_1 . The oscillations initially reach an amplitude of ± 0.35 rad.

2) *Step Down Change in Tie Line Impedance at High Load Imbalance:* Data is shown for a sudden change of the tie line impedance between area 1 and area 2 (closing of S_1 at $t = 40$ s). Fig. 6 shows the active power output of the VSMs. The change in tie line impedance from a high value to a low value triggers strong power oscillations between the two areas which are slowly increasing as long as the load imbalance persists and decay once balance between the two grids is restored (data not shown here). The amplitude of the frequency oscillations initially is ± 1 rad/s for this scenario (see Fig. 7). A slow decay of the system frequency is observed over the course of 20 s. When the VF is activated, frequency and active power outputs of the VSMs converge within 1s without oscillations.

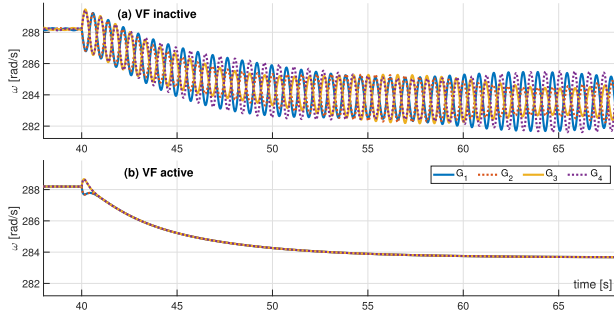


Fig. 7. Frequencies following a tie-line impedance step down starting at $t = 40$ s, at high load imbalance. (a) Oscillations increase slowly while the load imbalance persists. (b) Frequency differences quickly decay when VF is active. Steady state is reached after about 20s in both cases.

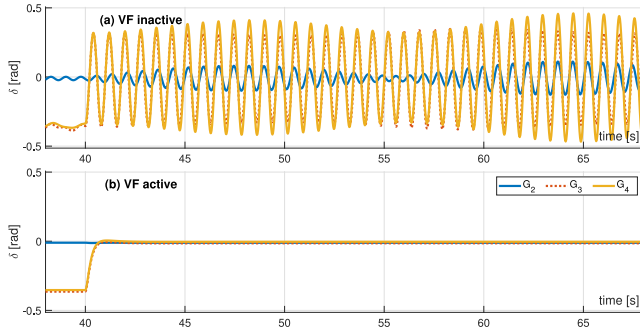


Fig. 8. Grounded rotor angles with respect to VSM G_1 , following a tie-line impedance step down starting at $t = 40$ s. (a) When VF is inactive, fast oscillations are amplitude modulated by a lower frequency component. (b) VF leads to a fast settling of the relative rotor angles.

The grounded angles of the four VSMs, shown in Fig. 8, have an angular difference of 0.35 rad before reconnection of tie line Y_5 , due to phase shift induced by the weak link between the two areas. In the absence of VF control, oscillations initially reach ± 0.35 rad and slowly increase over time. With VF, the grounded angles converge to zero within 2 seconds. The oscillations in this scenario are in the range of 1.2Hz and about twice as fast as in the first scenario.

Note that the steady state power output of the VSMs only depends on P_{set} and ω . With P_{set} being equal for all 4 VSMs, the active power outputs of the VSMs reach equal values even if the load is not balanced between the areas (see [25]). Note also, that the value for d is chosen relatively low and that stronger damping of course can also be achieved by increasing d . This however comes at the cost of requiring the VSMs to supply large excess power in the case of ω deviating from ω_{nom} . An adequate choice of d and f should be made such that for a given (micro)grid d can stabilize the grid in normal operation, while f helps improving the speed of convergence and decreases oscillations.

B. The Simplified Model (FEPS)

In order to see if we get comparable results for the simplified model (the FEPS model), we have computed the Y -matrices of the grid by network reduction from the parameters of the detailed model. In order to calculate a_{jk} , φ_{jk} and p_j , using the formulas in shown in IV, the VSM output voltages were

obtained from the stable equilibrium state of the VSM model used in the previous subsection, for each of the four states of the grid: S_1 open/closed and S_2 open/closed.

Load step changes and tie line step changes were simulated by switching between the corresponding Y -matrices according to the two scenarios shown in the previous subsection. Of course the simplified model does not contain time delays. For the case of load L_3 disconnected and a low tie line impedance (switch 1 closed) the parameters a_{jk} and φ_{jk} are:

$$a_{jk} = \begin{bmatrix} 0 & 68170 & 20009 & 13688 \\ 68170 & 0 & 29228 & 19995 \\ 20009 & 29228 & 0 & 68155 \\ 13688 & 19995 & 68155 & 0 \end{bmatrix},$$

$$\varphi_{jk} = \begin{bmatrix} -2.940 & 0.132 & 0.189 & 0.242 \\ 0.132 & -2.943 & 0.136 & 0.189 \\ 0.189 & 0.136 & -2.943 & 0.132 \\ 0.242 & 0.189 & 0.132 & -2.940 \end{bmatrix}.$$

For a high tie line impedance, all the values a_{jk} decrease significantly, however a_{12} and a_{34} increase:

$$a_{jk} = \begin{bmatrix} 0 & 86724 & 981 & 672 \\ 86724 & 0 & 1435 & 983 \\ 981 & 1435 & 0 & 78580 \\ 672 & 983 & 78580 & 0 \end{bmatrix}.$$

All the values φ_{jk} also increase with an increase in the tie line impedance, however the increase is smaller:

$$\varphi_{jk} = \begin{bmatrix} -2.945 & 0.144 & 0.209 & 0.262 \\ 0.144 & -2.924 & 0.156 & 0.209 \\ 0.209 & 0.156 & -2.924 & 0.144 \\ 0.262 & 0.209 & 0.144 & -2.945 \end{bmatrix}.$$

The values of a_{jk} decrease when load L_3 is connected for both high and low tie-line impedances, whereas absolute values of angles slightly increase when L_3 is connected at high tie-line impedance and absolute values of angles slightly decrease when L_3 is connected at low tie-line impedance. The stability criterion in Theorem 1 predicts stable operation of the model for a low tie line impedance. For L_3 disconnected, $\Gamma_{min} = 564\text{s}^{-1}$ and $\Gamma_{crit} = 394\text{s}^{-1}$, while for L_3 connected, $\Gamma_{min} = 549\text{s}^{-1}$ and $\Gamma_{crit} = 368\text{s}^{-1}$. This gives $\gamma_{min} = 42.7^\circ$ and $\gamma_{max} = 137.3^\circ$ and $\gamma_{min} = 40.8^\circ$ and $\gamma_{max} = 139.2^\circ$ respectively. At high tie line impedance, $\Gamma_{min} < \Gamma_{crit}$. This shows that the stability and synchronization criterion shown in the theorem is conservative, because the NRPS model shows stable behaviour even at high tie-line impedance. Note however that the detailed model was not stable at low tie-line impedance and high load imbalance. In the following the results of the simplified model can be seen to be stable for this case.

1) *Step Down Change in Load at High Tie Line Impedance:* Fig. 9 shows the frequencies of the 4 VSMs for a load step change of -5000 W in area 2. Starting at $t = 50$ s, the frequencies increase from below 299 rad/s to 311 rad/s. Inter area oscillations appear with a period of 1.5 s. VF efficiently damps these oscillations. (The convergence of the frequencies to the new higher value is faster than in the detailed model.)

Fig. 10 shows grounded rotor angles relative to G_1 . Here the NRPS model exhibits slightly higher amplitude than the

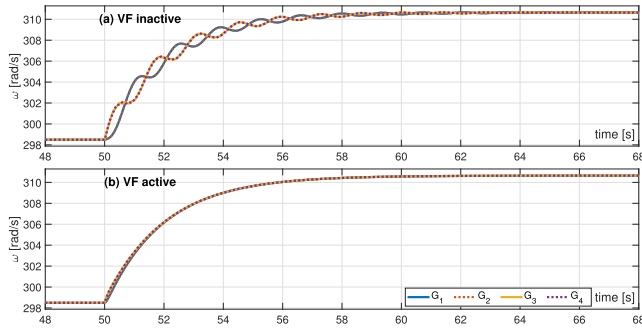


Fig. 9. Frequencies following the disconnection of load L_3 (starting from steady state) for the simplified model. (a) Behavior is similar to the detailed model with oscillations between the two areas. (b) Frequencies converge fast towards ω_c when VF is active.

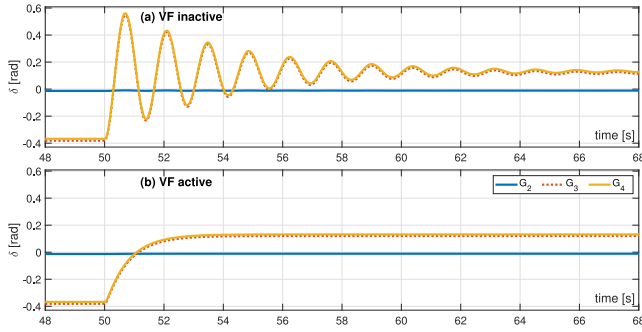


Fig. 10. Grounded rotor angles with respect to VSM G_1 following the disconnection of load L_3 (starting from steady state) for the simplified model. (a) The damped oscillations show in data for G_3 and G_4 . (b) VF leads to fast convergence of the grounded angles towards steady state.

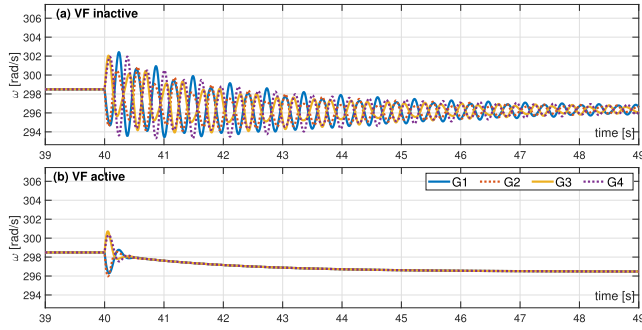


Fig. 11. Frequencies following a tie-line impedance step down at $t = 40s$ (starting from steady state). (a) Without VF, similar to the results with the detailed model, the simplified model shows several frequency components in the oscillations, however they are damped. (b) VF strongly damps these oscillations.

detailed model. Note that the grounded angles of G_3 and G_4 converge to approximately $+0.14$ rad/s, whereas in the detailed model this difference is close to zero.

2) *Step Down Change in Tie Line Impedance at High Load Imbalance:* We show results for the simplified model switching at $t = 40$ s from high to low tie line impedance while S_2 is closed. As in the detailed model, the change entails strong oscillations with frequencies around 3Hz, however the system is stable. VF damps the oscillations of the network efficiently as seen in Fig. 11b and Fig. 12b. A small overshoot can be observed shortly after $t = 40$ s.

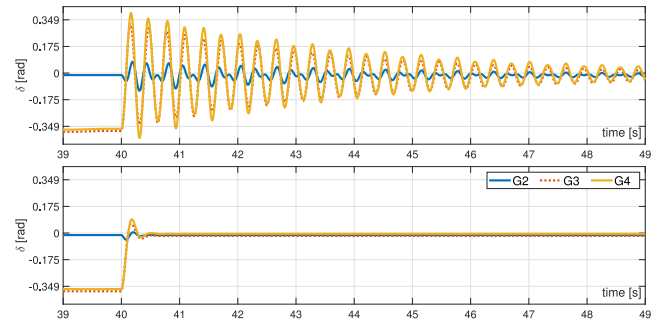


Fig. 12. Grounded rotor angles with respect to VSM G_1 following a tie-line impedance step down at $t = 40s$ (starting from steady state). (a) Oscillations decay slowly without VF. (b) The strong damping of VF is clearly visible, only a small overshoot occurs shortly after $t = 40s$.

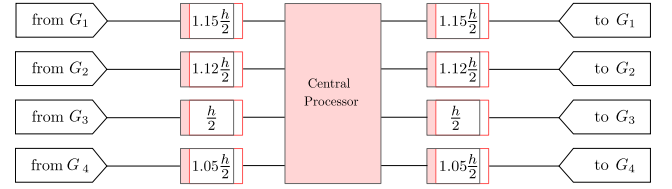


Fig. 13. System time delays for investigation of the influence of a delay in the VF calculation. Delay base value h as indicated in the text.

C. The Impact of Delays

We have performed simulations to investigate the influence of a communication time delay on our setup. The simulations were carried out with different (constant) time delays on the transmission of the rotor frequency of the 4 VSMs to the central unit and back. We ran simulations with uniform and non-uniform time delays in the system, with values ranging from 1ms to 5000ms. We have found that uniform time delays on all VSMs were slightly less perturbing than non-uniform time delays. As a representative result, we include here simulations with non-uniform but fixed time delays. Fig. 13 shows the time delays used between the VSMs and the central processing unit that calculates the COI frequency. The value h in this figure denotes the nominal round trip delay. All delay values given in the subsequent section refer to the value h as shown in Fig. 13.

Fig. 14 and Fig. 15 show rotor speed and power output of VSM G_1 for time delays between $h = 1ms$ and $h = 100ms$. The scenario for which data is shown here is explained in Table I. While for the value h between 1 – 10ms there is almost no impact on frequency and active power output, the frequency change following disturbances for $h > 10ms$ becomes slower. This is visible in a lower frequency dip after grid connection of the VSMs initially and a slower convergence towards the equilibrium frequency after the disconnection of L_3 at $t = 30s$. The power output shows a higher peak upon grid connection of the inverters, which is induced by the slower system behaviour. The active power output subsequent to grid disturbances at $t = 20s$ and $t = 30s$ does not significantly differ for different time delays in Fig. 14.

Fig. 16 and Fig. 17 show results for the same scenario, but with time delays h between 200ms and 5000ms, which affect the behaviour of the VSMs. While at 200ms the frequency of G_1 changes slower but smoothly following grid connection

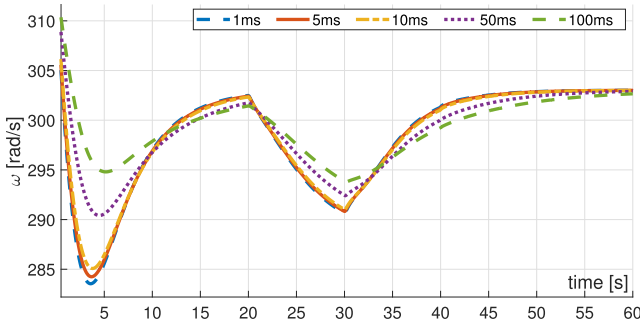


Fig. 14. Frequency of VSM G_1 with time delays h between $1ms$ and $100ms$. The convergence to a new steady state gets increasingly slow for higher delays.

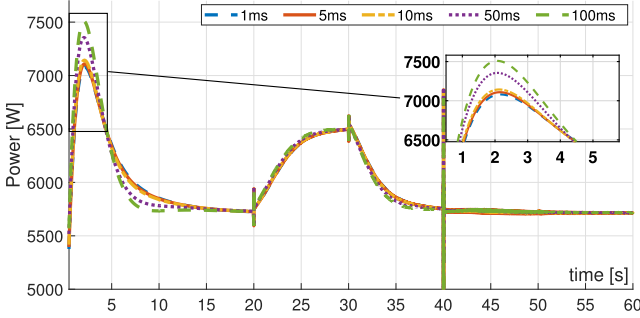


Fig. 15. Active power output of VSM G_1 with time delays h between $1ms$ and $100ms$, with a zoom of the first 5s. For higher delays, the initial peak after connection becomes more pronounced.

TABLE I
EVENTS IN THE GRID

Time	Event
0s	Startup and synchronization of the VSMs
10s	Tie line impedance increases (Switch S_1 opens)
20s	Step increase of the load in area 2 (Switch S_2 closes)
30s	Step decrease of the load in area 2 (Switch S_2 opens)
40s	A $2ms$ three phase fault occurs (Switch S_3 closes for $2ms$)
50s	Tie line impedance decreases (Switch S_1 closes)
60s	End of simulation

and disturbances, a delay of $500ms$ induces ripples after grid connection of the inverter. Higher delays cause significant disturbances that are slowly washing out and decaying over the simulation time. Active power output in Fig. 17 shows little disturbances and differences for $h = 200ms$ and $h = 500ms$, but ripples and excursions from the normal behaviour get stronger for increasing time delays. At $h = 5000ms$, the highest disturbance at $6s$ reaches an amplitude of $1000W$.

The above results are a small representative subset of simulations that were computed for a fine-grained set of delays. Simulations with other time delays support the results shown here. Impact of delays on VSMs G_2 to G_4 are similar to the results shown for VSM G_1 . Overall it can be said that for time delays below $10ms$, system behaviour remains almost unchanged, whereas time delays up to $100ms$ slow down frequency response to some extent, but do not significantly impact the VSM power output once the VSMs are fully started. For time delays above $500ms$, the system behaviour deteriorates in response speed and delay values above $1000ms$ induce slowly decaying disturbances following rapid changes in grid

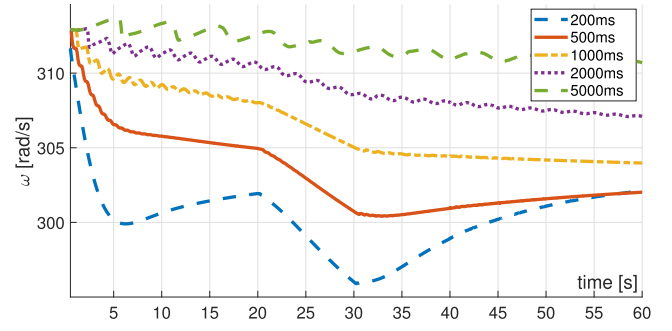


Fig. 16. Frequency of VSM G_1 with time delays h between $200ms$ and $5000ms$. For delays over $200ms$ nonlinear, decaying oscillations are visible following VSM connection.

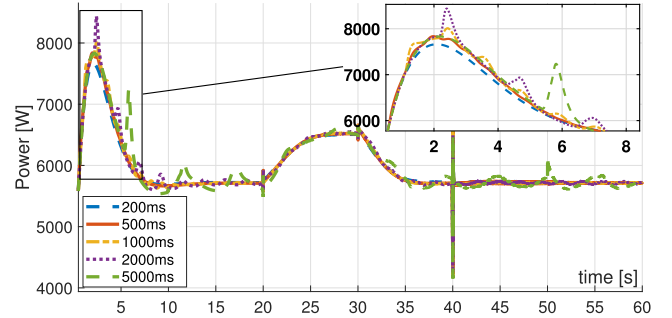


Fig. 17. Active power output of G_1 with time delays h between $200ms$ and $5000ms$, with a zoom of the first 8s. For time delays above $200ms$ disturbances clearly show.

conditions. However inter area oscillations are damped out at all delay values.

VI. CONCLUSION

This paper provides a proof of the stability of the NRPS model when employing VF, leading to the FEPS model. A singular perturbation analysis of the FEPS model shows that the same stability boundaries apply as in [37], however, the new result does not require to work with very small inertia. Our theoretical results are supported by simulations of the NRPS and FEPS models for a small grid comprising four VSMs of $9kW$ each. Comparison with the simulations of the detailed model shows good agreement, both with and without VF. In both cases VF was highly effective in damping oscillations. For a VF coefficient of $F_j = 3141.6Ws$, the system showed transients decaying within 1-2 seconds. Furthermore, simulations with different time delays indicate that the VF mechanism remains effective in damping inter area oscillations also for higher time delays. In particular the system behaviour remains good for non-uniform constant time delays up to $100ms$.

REFERENCES

- [1] O. Ajala, A. Domínguez-García, P. Sauer, and D. Liberzon, "A second-order synchronous machine model for multi-swing stability analysis," in *Proc. IEEE North Amer. Power Symp. (NAPS)*, Wichita, KS, USA, 2019, pp. 1–6.
- [2] J. Alipoor, Y. Miura, and T. Ise, "Distributed generation grid integration using virtual synchronous generator with adaptive virtual inertia," in *Proc. IEEE Energy Convers. Congr. Expo.*, Denver, CO, USA, 2013, pp. 4546–4552.
- [3] R. Aouini, B. Marinescu, K. B. Kilani, and M. Elleuch, "Synchronverter-based emulation and control of HVDC transmission," *IEEE Trans. Power Syst.*, vol. 31, no. 1, pp. 278–286, Jan. 2016.

- [4] C. Arghir, T. Jouini, and F. Dörfler, "Grid-forming control for power converters based on matching of synchronous machines," *Automatica*, vol. 95, pp. 273–282, Sep. 2018.
- [5] S. Baros, C. N. Hadjicostis, and F. O'Sullivan, "Stability analysis of droop-controlled inverter-based power grids via timescale separation," in *Proc. 59th IEEE Conf. Decis. Control (CDC)*, 2020, pp. 2098–2104.
- [6] H.-P. Beck and R. Hesse, "Virtual synchronous machine," in *Proc. IEEE 9th Int. Conf. Electr. Power Qual. Utilisation*, Barcelona, Spain, 2007.
- [7] M. Blau and G. Weiss, "Synchronverters used for damping inter-area oscillations in two-area power systems," in *Proc. Int. Conf. Renew. Energies Power Qual. (ICREPQ)*, 2018, pp. 45–50.
- [8] D. Casagrande, A. Astolfi, R. Ortega, and D. Langarica, "A solution to the problem of transient stability of multimachine power systems," in *Proc. 51st IEEE Conf. Decis. Control (CDC)*, 2012, pp. 1703–1708.
- [9] M. Chen, D. Zhou, and F. Laabjerg, "Active power oscillation damping based on acceleration control in parallel virtual synchronous generators system," *IEEE Trans. Power Electron.*, vol. 36, no. 8, pp. 9501–9510, Aug. 2021.
- [10] H. D. Chiang, *Direct Methods for Stability Analysis of Electric Power Systems: Theoretical Foundation, BCU Methodologies, and Applications*. Hoboken, NJ, USA: Wiley, 2011.
- [11] H.-D. Chiang and C.-C. Chu, "Theoretical foundation of the BCU method for direct stability analysis of network-reduction power system. Models with small transfer conductances," *IEEE Trans. Circuits Syst. I, Fundam. Theory Appl.*, vol. 42, no. 5, pp. 252–265, May 1995.
- [12] M. Choopani, S. H. Hosseinian, and B. Vahidi, "A novel comprehensive method to enhance stability of multi-VSG grids," *Int. J. Electr. Power Energy Syst.*, vol. 104, pp. 502–514, Jan. 2019.
- [13] C. De Persis and N. Monshizadeh, "Bregman storage functions for microgrid control," *IEEE Trans. Autom. Control*, vol. 63, no. 1, pp. 53–68, Jan. 2018.
- [14] G. Delille, B. François, and G. Malarange, "Dynamic frequency control support: A virtual inertia provided by distributed energy storage to isolated power systems," in *Proc. IEEE PES Innovative Smart Grid Technol. Conf. Europe (ISGT Europe)*, 2010, pp. 1–8.
- [15] F. Dörfler and F. Bullo, "Synchronization and transient stability in power networks and nonuniform Kuramoto oscillators," *SIAM J. Control Optim.*, vol. 50, no. 3, pp. 1616–1642, 2012.
- [16] F. Dörfler and F. Bullo, "Synchronization in complex networks of phase oscillators: A survey," *Automatica*, vol. 50, no. 6, pp. 1539–1564, 2014.
- [17] J. Driesen and K. Visscher, "Virtual synchronous generators," in *Proc. IEEE Power Energy Soc. Gen. Meeting-Convers. Del. Electr. Energy 21st Century*, Pittsburgh, PA, USA, 2008.
- [18] S. Jafarpour and F. Bullo, "Synchronization of Kuramoto oscillators via cutset projections," *IEEE Trans. Autom. Control*, vol. 64, no. 7, pp. 2830–2844, Jul. 2019.
- [19] Z. Kustanovich, F. Reissner, S. Shivratri, and G. Weiss, "The sensitivity of grid-connected synchronverters with respect to measurement errors," *IEEE Access*, vol. 9, pp. 118985–118995, 2021.
- [20] Z. Kustanovich, S. Shivratri, and G. Weiss, "Virtual synchronous machines with fast current loop and secondary control," in *Proc. 21st IFAC World Congr.*, Berlin, Germany, Jul. 2020.
- [21] Z. Kustanovich and G. Weiss, "Synchronverter based photovoltaic inverter," in *Proc. IEEE Int. Conf. Sci. Electr. Eng.*, 2018, pp. 1–5.
- [22] F. Mandrile, "Next generation inverters equipped with virtual synchronous compensators for grid services and grid support," Ph.D. dissertation, DENERG, Politecnico di Torino, Turin, Italy, Nov. 2020.
- [23] F. Mandrile, E. Carpaneto, and R. Bojoi, "Grid-feeding inverter with simplified virtual synchronous compensator providing grid services and grid support," *IEEE Trans. Ind. Appl.*, vol. 57, no. 1, pp. 559–569, Jan./Feb. 2021.
- [24] J. Morren, S. W. H. De Haan, W. L. Kling, and J. A. Ferreira, "Wind turbines emulating inertia and supporting primary frequency control," *IEEE Trans. Power Syst.*, vol. 21, no. 1, pp. 433–434, Feb. 2006.
- [25] V. Natarajan and G. Weiss, "Synchronverters with better stability due to virtual inductors, virtual capacitors, and anti-windup," *IEEE Trans. Ind. Electron.*, vol. 64, no. 7, pp. 5994–6004, Jul. 2017.
- [26] C. P. Nguyen and A. J. Flueck, "Modeling of communication latency in smart grid," in *Proc. IEEE Power Energy Soc. Gen. Meeting*, Detroit, MI, USA, 2011, pp. 1–7.
- [27] Y. Ojo, J. Watson, and I. Lestas, "A review of reduced-order models for microgrids: Simplifications vs accuracy," 2020, *arXiv:2003.04923*.
- [28] J. Roldán-Pérez, A. Rodríguez-Cabero, and M. Prodanovic, "Parallel current-controlled synchronverters for voltage and frequency regulation in weak grids," *J. Eng.*, vol. 2019, no. 17, pp. 3516–3520, 2019.
- [29] R. Rosso, S. Engelken, and M. Liserre, "Robust stability analysis of synchronverters operating in parallel," *IEEE Trans. Power Electron.*, vol. 34, no. 11, pp. 11309–11319, Nov. 2019.
- [30] P. Sauer and M. Pai, *Power System Dynamics and Stability*. Champaign, IL, USA: Stipes Publ. LLC, 1997.
- [31] K. Smith, S. Jafarpour, and F. Bullo, "Transient stability of droop-controlled inverter networks with operating constraints," *IEEE Trans. Autom. Control*, early access, Jan. 25, 2021, doi: [10.1109/TAC.2021.3053552](https://doi.org/10.1109/TAC.2021.3053552).
- [32] A. Tayyebi, A. Anta, and F. Dörfler, "Almost globally stable grid-forming hybrid angle control," in *Proc. 59th IEEE Conf. Decis. Control (CDC)*, 2020, pp. 830–835.
- [33] A. Tayyebi, A. Anta, and F. Dörfler, "Hybrid angle control and almost global stability of grid-forming power converters," 2020, *arXiv:2008.07661*.
- [34] A. Tayyebi, D. Groß, A. Anta, F. Kupzog, and F. Dörfler, "Frequency stability of synchronous machines and grid-forming power converters," *IEEE J. Emerg. Sel. Topics Power Electron.*, vol. 8, no. 2, pp. 1004–1018, Jun. 2020.
- [35] K. R. Vasudevan, V. K. Ramachandaramurthy, T. S. Babu, and A. Pouryekt, "Synchronverter: A comprehensive review of modifications, stability assessment, applications and future perspectives," *IEEE Access*, vol. 8, pp. 131565–131589, 2020.
- [36] P. Vorobev, P. H. Huang, M. Al Hosani, J. L. Kirtley, and K. Turitsyn, "High-fidelity model order reduction for microgrids stability assessment," *IEEE Trans. Power Syst.*, vol. 33, no. 1, pp. 874–887, Jan. 2018.
- [37] G. Weiss, F. Dörfler, and Y. Levron, "A stability theorem for networks containing synchronous generators," *Syst. Control Lett.*, vol. 134, Dec. 2019, Art. no. 104561.
- [38] G. Weiss and E. Venezan, "Stability analysis for coupled synchronous generators with virtual friction," in *Proc. 22d Int. Conf. Digit. Signal Process. (DSP)*, 2017, pp. 1–5.
- [39] L. Wu and H. Chen, "Synchronization conditions for a third-order Kuramoto network," in *Proc. 59th IEEE Conf. Decis. Control (CDC)*, 2020, pp. 5834–5839.
- [40] B. Yang, K. V. Katsaros, W. K. Chai, and G. Pavlou, "Cost-efficient low latency communication infrastructure for synchrophasor applications in smart grids," *IEEE Syst. J.*, vol. 12, no. 1, pp. 948–958, Mar. 2018.
- [41] N. Zargari, R. Ofir, Y. Levron, and J. Belikov, "Using DQ0 signals based on the central angle reference frame to model the dynamics of large-scale power systems," in *Proc. IEEE PES Innovative Smart Grid Technol. Europe (ISGT-Europe)*, Delft, The Netherlands, 2020, pp. 1099–1103.
- [42] Q. C. Zhong, P. L. Nguyen, Z. Ma, and W. Sheng, "Self-synchronized synchronverters: Inverters without a dedicated synchronization unit," *IEEE Trans. Power Electron.*, vol. 29, no. 2, pp. 617–630, Feb. 2014.
- [43] Q. C. Zhong and G. Weiss, "Synchronverters: Inverters that mimic synchronous generators," *IEEE Trans. Ind. Electron.*, vol. 58, no. 4, pp. 1259–1267, Apr. 2011.

Florian Reissner received the B.Sc. and M.Sc. degrees from Technical University Berlin, Germany, in 2015. He is currently pursuing the Ph.D. degree with the Power Electronics for Renewable Energy Group, Tel Aviv University. From 2015 to 2020, he worked in project management with Vinci Energies, Lyon, and as innovation consultant in incubators in Frankfurt and Berlin. His current research interests include control techniques in power systems and control theory.

Hang Yin received the B.Sc. degree in instrument engineering from the North University of China, Taiyuan, China, in 2014, and the M.Sc. degree in astronomy instruments from the University of Chinese Academy of Sciences, Beijing, China, in 2017. He is currently pursuing the Doctoral degree in electrical engineering with Tel Aviv University, Israel. His research interests include power electronics and power systems.

George Weiss received the M.Eng. degree in control engineering from the Polytechnic Institute of Bucharest, Romania, in 1981, and the Ph.D. degree in applied mathematics from the Weizmann Institute, Rehovot, Israel, in 1989. He was with Brown University, Providence, RI, USA; Virginia Tech, Blacksburg, VA, USA; Ben-Gurion University, Beer Sheva, Israel; the University of Exeter, U.K.; and Imperial College London, U.K. He is leading research projects for the European Commission and for the Israeli Ministry of Energy. His current research interests include distributed parameter systems, operator semigroups, passive and conservative systems (linear and nonlinear), power electronics, microgrids, repetitive control, sampled data systems, and wind-driven power generators.